Springer

KSME

Journal of Mechanical Science and Technology 33 (2) (2019) 889~902
www.springerlink.com/content/1738-494x(Print)/1976-3824(Online)
DOI 10.1007/s12206-019-0146-z

Kinematic performance analysis and promotion of a spatial 3-RPaS parallel manipulator with multiple actuation modes †

Liping Wang[1,2], Zhaokun Zhang[1,2] and Zhufeng Shao[1,2,*]

[1]*Beijing Key Lab of Precision/Ultra-Precision Manufacturing Equipment and Control, Tsinghua University, Beijing 100084, China*
[2]*State Key Laboratory of Tribology & Institute of Manufacturing Engineering, Department of Mechanical Engineering, Tsinghua University, Beijing 100084, China*

(Manuscript Received June 16, 2018; Revised October 14, 2018; Accepted October 29, 2018)

Abstract

This paper presents a 3-RPaS (R and S denote the revolute and spherical joint, pa denotes the parallelogram) parallel manipulator with two-rotational-degrees-of-freedom (2R1T) and one-translational-degree-of-freedom motion. By introducing parallelograms and an innovative driving module, the 3-RPaS manipulator can change the transmission path of the driving and reaction forces, and achieves 27 actuation modes. The kinematic performance of the manipulator under different actuation modes is analyzed with the indices that are defined based on matrix orthogonal degree. Comparative analysis indicates that the kinematic performance of the manipulator varies significantly in different actuation modes. A reasonable selection of actuation modes can effectively improve the kinematic performance and eliminate singularities. The concept of optimal actuation mode and the implementation approach of actuation mode conversion are discussed and analyzed for kinematics promotion. The kinematic performance of the manipulator is greatly improved with optimal actuation modes, without changing the topology structure and dimensional parameters.

Keywords: 2R1T parallel manipulator; Actuation mode; Kinematics promotion; Performance index

1. Introduction

Parallel manipulators (PMs) have received extensive academic attention because of their distinctive advantages, such as high stiffness, high precision, high load capability and good dynamics [1, 2]. PMs with six degrees of freedom (DOFs) have the insurmountable disadvantages of small workspace and complex singularity. In practical applications, lower-mobility PMs are mostly used due to their expanded workspace and improved performance, such as the commercialized Delta robot [3] and sprint Z3 tool head [4]. In particular, PMs with two-rotational-degrees-of-freedom and one-translational-degree-of-freedom (2R1T) are a kind of lower-mobility PM and have been widely used in tool heads [5-7], solar trackers [8], motion simulators [9], micromanipulators [10], and measuring machines [11].

Extensive research has been carried out on the type synthesis, performance analysis and optimization of 2R1T PMs. Song [12] proposed an analytical method based on conformal geometrical algebra to implement and unify type synthesis of 2R1T PMs. Xu [13] obtained 3UPS-UP, 2UPS-UP, and 2UPR-SPR 2R1T PMs with two continuous rotational axes by screw theory and space geometry. Xu [14] proposed a 2R1T PM with minimum DOF of joints and fixed linear actuators. Hu [15] proposed a family of 2R1T PMs with intersecting rotational axes. Xu [16] presents a novel 2-RPU/SPR 2R1T PM. Here, the notation of R, P, U and S denotes the revolute, prismatic, universal, and spherical joint, respectively. To improve the kinematic performance of 2R1T PMs, the approach of redundancy is most commonly used [17, 18]. However, redundancy results in complex control and serious coupling of internal forces [19]. Dimensional optimization is another widely adopted approach to improve the kinematic performance of PMs [20]. Recently, variable actuated parallel manipulators (VAPMs) have been proposed and applied to improve the performance of planar PMs [21-23]. A VAPM has a variety of available actuation modes. By converting its actuation modes, a VAPM achieves the variation and promotion on kinematics without redundancy and change on the configuration. This gives VAPMs an important research value that deserves further study.

Performance indices are the basis for the performance analysis and optimization of PMs. In terms of kinematics, there are mainly two categories [24]: The indices based on the Jacobian matrix and the motion/force transmission indices based on the screw theory. In the first category, indices such

*Corresponding author. Tel.: +86 10 62794598
E-mail address: shaozf@mail.tsinghua.edu.cn
† Recommended by Associate Editor Baek-kyu Cho

as manipulability [25], the local conditioning index (LCI) [26], and the global conditioning index (GCI) [27] have been proposed and widely used. However, the performance indices based on the Jacobian matrix cannot be applied to PMs with mixed DOFs due to the dimensional inconsistency of Jacobian matrices [28]. Liu [29] further found that LCI could converge and it is dependent on the coordinate systems. The motion/force transmission indices based on screw theory are derived from the concept of the virtual coefficient proposed by Ball [30] and are used to describe the instantaneous work efficiency between the transmission wrench screw and the output twist screw. Yuan [31], Sutherland [32], Tsai [33, 34], and Chen [35] proposed different transmission indices. Wang, et al. [36] established systematic indices to evaluate the motion/force transmissibility of PMs. The screw theory is a powerful mathematical tool, but the calculation is complex. Shao, et al. [37] established a transmission index based on the matrix orthogonal degree, which is concise and versatile with simple calculation as well as clear physical meaning. The matrix-orthogonal-degree-based indices indicate good application potential and are improved and adopted for the analysis of VAPMs in this study.

This paper presents a novel spatial 3-RPaS (Pa denotes the parallelogram) 2R1T PM with 27 actuation modes. Based on the kinematic performance analysis of the 3-RPaS PM under different actuation modes, the approach of actuation mode conversion is discussed to improve the kinematic performance. The remaining content of the paper is as follows: Sec. 2 introduces the 3-RPaS manipulator and its achievable actuation modes. Sec. 3 establishes the inverse kinematic model for the 3-RPaS manipulator. Sec. 4 defines the transmission indices based on matrix orthogonal degree and determines the calculation method. Sec. 5 analyzes and compares the kinematic performance of the 3-RPaS manipulator under various actuation modes. Sec. 6 discusses the approach to improve kinematic performance by actuation mode conversion. Sec. 7 gives the conclusions.

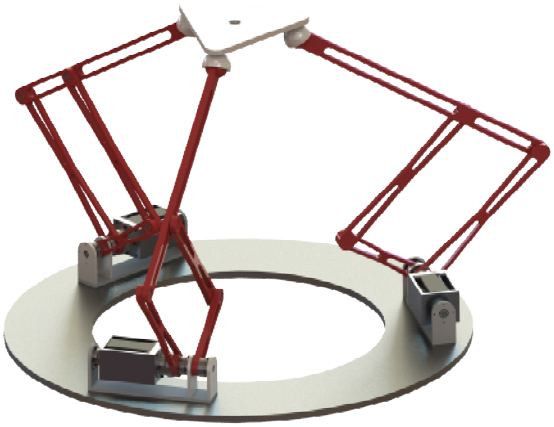

(a) Virtual prototype of the 3-RPaS PM

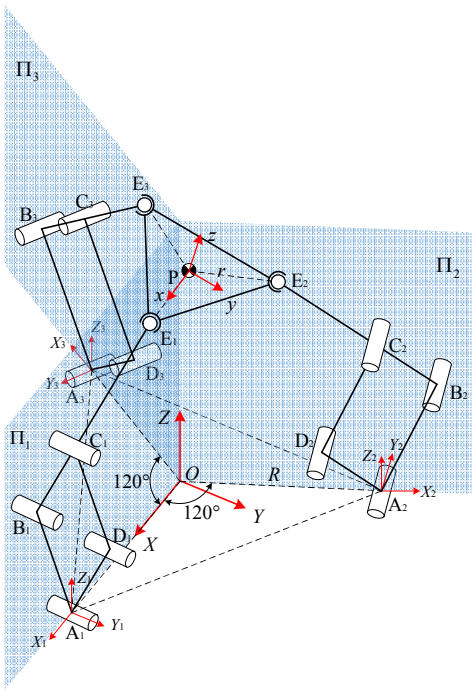

(b) Schematic diagram of the 3-RPaS PM

Fig. 1. Spatial 3-RPaS parallel manipulator with multiple actuation modes.

2. 3-RPaS parallel manipulator with multiple actuation modes

The virtual prototype of the proposed spatial 3-RPaS PM is shown in Fig. 1(a), and its schematic diagram is shown in Fig. 1(b). The spatial 3-RPaS PM consists of three RPaS branch chains connecting the base and the end effector in parallel. Branches are arranged symmetrically on the circumference and located in three vertical planes (Π_1, Π_2 and Π_3). An RPaS branch chain consists of four links (A_iB_i, A_iD_i, D_iC_i and B_iE_i), five revolute joints and one spherical joint. It should be noted that there are two collinear revolute joints on A_i, which connect link A_iB_i and A_iD_i respectively. Links A_iB_i and D_iC_i are equal in length and parallel to each other, forming the parallelogram $A_iB_iC_iD_i$. The branch is connected to the end effector via a spherical joint E_i. The 3- RPaS PM is equivalent to the 3-RRS PM [38] in terms of the mobility, which produces 2R1T motion.

The RPaS branch has two configurations, as shown in Fig. 2.

The configuration of Fig. 2(a) is called the inner type, and the parallelogram locates inside the branch. In contrast, the parallelogram in Fig. 2(b) locates outside the branch, and it is named the outer type. The two topological configurations are equivalent in kinematics. In this study, the 3-RPaS manipulator with inner type chains is analyzed. The links in the RPaS branch are arranged in four layers (see Fig. 1(a)) to avoid interference between links. Therefore, the motion range of the branch chain is greatly increased.

A servomotor drives the RPaS branch. To reduce the moving inertia, the servomotor is placed at A_i. Three actuation methods of the RPaS branch can be obtained by applying the

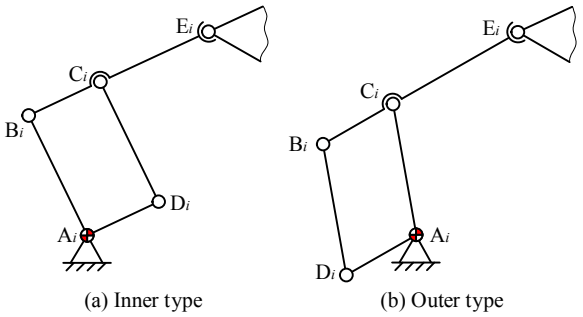

Fig. 2. Two topological configurations of the RPaS branch chain.

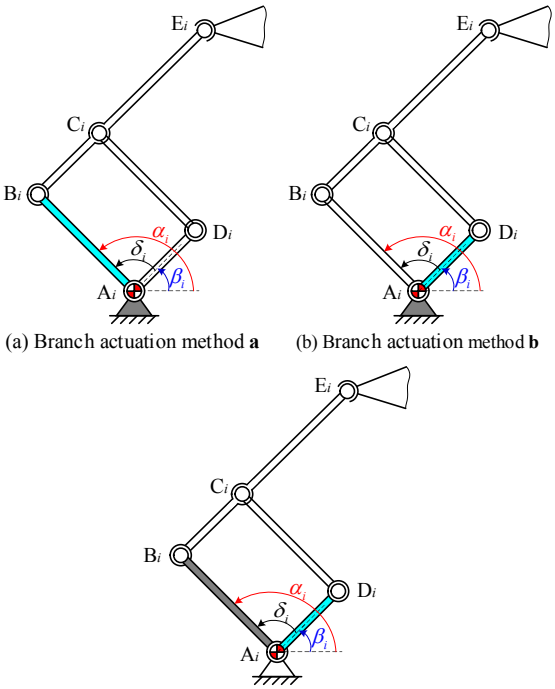

Fig. 3. Three actuation methods for the RPaS branch chain.

driving and reaction forces to different links of the parallelogram, as shown in Fig. 3.

Branch actuation method **a**: If the motor shell is fixed with the base while the output shaft is connected with link A_iB_i, the output torque is exerted on link A_iB_i to rotate it about joint A_i. The reaction torque is directly exerted on the base. Link A_iB_i is actuated and the other links are passive. The input variable is the rotation angle α_i of link A_iB_i, as shown in Fig. 3(a).

Branch actuation method **b**: If the motor shell is fixed with the base while the output shaft is connected with link A_iD_i, the output torque is exerted on link A_iD_i to rotate it about joint A_i. The reaction torque is directly exerted on the base. Link A_iD_i is actuated and the other links are passive. The input variable is the rotation angle β_i of link A_iD_i, as shown in Fig. 3(b).

Branch actuation method **c**: If the motor shell is fixed with link A_iB_i while the output shaft is connected with link A_iD_i, the output torque is exerted on link A_iD_i while the reaction torque is transmitted to link A_iB_i. Both A_iB_i and A_iD_i are active and actuated to rotate about joint A_i with respect to each other. The input variable is the relative rotation angle δ_i of links A_iB_i and A_iD_i, as shown in Fig. 3(c).

A single RPaS branch can employ any of the three actuation methods during work. A combination of branch actuation methods represents a choice for the actuation scheme, which is called an actuation mode of the 3-RPaS manipulator. Therefore, 27 actuation modes are available, as listed in Table 1. Considering the circular symmetry, some actuation modes are equivalent and can be classified into one category. For example, modes 6, 16 and 20 belong to the same category. Finally, eleven categories of actuation modes for the 3-RPaS manipulator are obtained and listed in Table 2.

Table 1. Twenty-seven actuation modes available for the 3-RPaS PM.

No	Combination	No	Combination	No	Combination
1	a-a-a	10	b-a-a	19	c-a-a
2	a-a-b	11	b-a-b	20	c-a-b
3	a-a-c	12	b-a-c	21	c-a-c
4	a-b-a	13	b-b-a	22	c-b-a
5	a-b-b	14	b-b-b	23	c-b-b
6	a-b-c	15	b-b-c	24	c-b-c
7	a-c-a	16	b-c-a	25	c-c-a
8	a-c-b	17	b-c-b	26	c-c-b
9	a-c-c	18	b-c-c	27	c-c-c

Table 2. Eleven categories of actuation modes for the 3-RPaS PM.

Mode number	Combinations of branch actuation methods	Input variables
I	a-a-a	$[\alpha_1\ \alpha_2\ \alpha_3]$
II	a-a-b (a-b-a, b-a-a)	$[\alpha_1\ \alpha_2\ \beta_3]$
III	a-a-c (a-c-a, c-a-a)	$[\alpha_1\ \alpha_2\ \delta_3]$
IV	a-b-b (b-b-a, b-a-b)	$[\alpha_1\ \beta_2\ \beta_3]$
V	a-b-c (b-c-a, c-a-b)	$[\alpha_1\ \beta_2\ \delta_3]$
VI	a-c-b (c-b-a, b-a-c)	$[\alpha_1\ \delta_2\ \beta_3]$
VII	a-c-c (c-c-a, c-a-c)	$[\alpha_1\ \delta_2\ \delta_3]$
VIII	b-b-b	$[\beta_1\ \beta_2\ \beta_3]$
IX	b-b-c (b-c-b, c-b-b)	$[\beta_1\ \beta_2\ \delta_3]$
X	b-c-c (c-c-b, c-b-c)	$[\beta_1\ \delta_2\ \delta_3]$
XI	c-c-c	$[\delta_1\ \delta_2\ \delta_3]$

3. Kinematic modeling of the 3-RPaS parallel manipulator

Fig. 4 illustrates the kinematics and the vector loop of the 3-RPaS manipulator. The fixed base $A_1A_2A_3$ is an equilateral

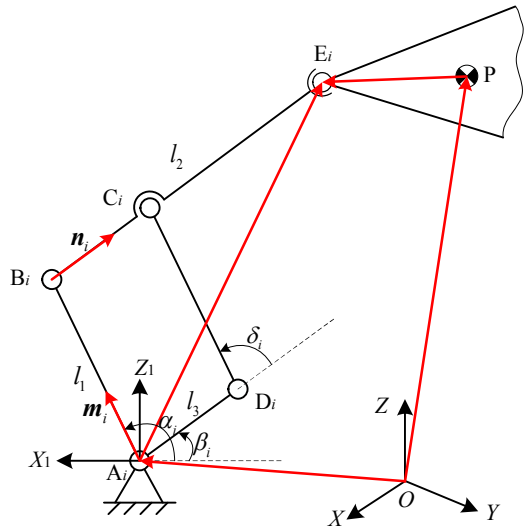

Fig. 4. Kinematic diagram and vector loop of the 3-RPaS manipulator.

triangle, and the circumcircle radius is R. The end effector $E_1E_2E_3$ is also an equilateral triangle with circumcircle radius r. The length of link A_iB_i is l_1, the length of link B_iE_i is l_2, and the length of link A_iD_i is l_3. A global coordinate system $\{O\text{-}XYZ\}$ is established at point O, where the X-axis is collinear with OA_1; the Z-axis is vertically upward, and the Y-axis is parallel to A_3A_2. A local coordinate system $\{P\text{-}xyz\}$ is established at point P and fixed with the end effector. The x-axis is collinear with PE_1; the z-axis is perpendicular to the end effector, and the y-axis is parallel to E_3E_2. $\boldsymbol{m}_i$ and $\boldsymbol{n}_i$ denote the unit direction vectors along links A_iB_i and B_iE_i, respectively.

The position vector of the end effector is $\boldsymbol{p}=\begin{bmatrix}X_P & Y_P & Z_P\end{bmatrix}^{\mathrm{T}}$. The position vectors $\boldsymbol{a}_i$ of joints A_i in the global coordinate system are

$$\begin{aligned}\boldsymbol{a}_1&=\begin{bmatrix}R & 0 & 0\end{bmatrix}^{\mathrm{T}}\\ \boldsymbol{a}_2&=\begin{bmatrix}-\frac{R}{2} & \frac{\sqrt{3}R}{2} & 0\end{bmatrix}^{\mathrm{T}}\\ \boldsymbol{a}_3&=\begin{bmatrix}-\frac{R}{2} & -\frac{\sqrt{3}R}{2} & 0\end{bmatrix}^{\mathrm{T}}.\end{aligned}\tag{1}$$

The position vectors ${}^{P}\boldsymbol{e}_i$ of joints E_i in the local coordinate system are:

$$\begin{aligned}{}^{P}\boldsymbol{e}_1&=\begin{bmatrix}r & 0 & 0\end{bmatrix}^{\mathrm{T}}\\ {}^{P}\boldsymbol{e}_2&=\begin{bmatrix}-\frac{r}{2} & \frac{\sqrt{3}r}{2} & 0\end{bmatrix}^{\mathrm{T}}\\ {}^{P}\boldsymbol{e}_3&=\begin{bmatrix}-\frac{r}{2} & -\frac{\sqrt{3}r}{2} & 0\end{bmatrix}^{\mathrm{T}}.\end{aligned}\tag{2}$$

The 3-RPaS manipulator is a 3-[PP]S mechanism [39], since the vertices E_1, E_2 and E_3 of the end effector always locate in the three vertical planes. The orientation of its end effector can be described by Tilt-and-Torsion (T&T) angles for convenience [39]. As shown in Fig. 5(a), $\boldsymbol{h}$ represents the normal vector of the end effector. Since the end effector has no torsion about vector $\boldsymbol{h}$, the orientation of the end effector can be uniquely determined by the azimuth angle φ and tilt angle θ of $\boldsymbol{h}$. Moreover, the orientation workspace of the manipulator can be represented by the polar coordinates shown in Fig. 5(b). The rotation matrix of the end effector with respect to the global coordinate system is

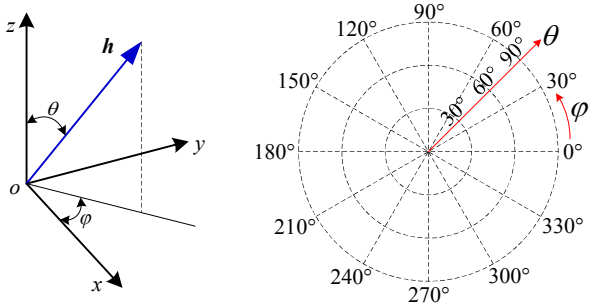

(a) T&T angles (b) Orientation workspace

Fig. 5. Orientation description and the orientation workspace by the T&T angles.

$$\begin{aligned}{}^{O}\boldsymbol{R}_P&=\boldsymbol{R}(z,\varphi)\boldsymbol{R}(y,\theta)\boldsymbol{R}(z,-\varphi)\\&=\begin{bmatrix}c^2\varphi c\theta+s^2\varphi & s\varphi c\varphi(c\theta-1) & c\varphi s\theta\\ s\varphi c\varphi(c\theta-1) & s^2\varphi c\theta+c^2\varphi & s\varphi s\theta\\ -c\varphi s\theta & -s\varphi s\theta & c\theta\end{bmatrix}\end{aligned}\tag{3}$$

where $s\varphi$ denotes $\sin\varphi$ and $c\varphi$ denotes $\cos\varphi$. The position vector of joint E_i in the global coordinate system is

$$\boldsymbol{e}_i=\boldsymbol{p}+{}^{O}\boldsymbol{R}_P\,{}^{P}\boldsymbol{e}_i.\tag{4}$$

Due to the geometric constraints that the vertices E_1, E_2 and E_3 of the end effector always locate in the three vertical planes, the following geometrical constraints are obtained:

$$\begin{cases}Y_{E1}=0\\ Y_{E2}=-\sqrt{3}X_{E2}\\ Y_{E3}=\sqrt{3}X_{E3}.\end{cases}\tag{5}$$

Considering Eqs. (2)-(5) together yields

$$\begin{aligned}X_P&=-\frac{r}{2}\cos 2\varphi(1-\cos\theta)\\ Y_P&=\frac{r}{2}\sin 2\varphi(1-\cos\theta).\end{aligned}\tag{6}$$

Since the manipulator only has 2R1T DOFs, the translational motions in the X and Y directions are regarded as para-

sitic motions.

For the ith branch chain (i = 1, 2, 3), a local coordinate system $\{A_i\text{-}X_iY_iZ_i\}$ is established at joint A_i. The X_i-axis is collinear with OA_i; the Z_i-axis is vertically upward, and the Y_i-axis is determined by the right-hand rule. The rotation matrix of the local coordinate system $\{A_i\text{-}X_iY_iZ_i\}$ with respect to the global coordinate system $\{O\text{-}XYZ\}$ is

$$ {}^{O}\boldsymbol{R}_i = \boldsymbol{R}\left(z,\psi_i\right) = \begin{bmatrix} \cos\psi_i & -\sin\psi_i & 0 \\ \sin\psi_i & \cos\psi_i & 0 \\ 0 & 0 & 1 \end{bmatrix} \tag{7} $$

where $\psi_i = 2i\pi/3,\ (i = 1,2,3)$. The vector $\overrightarrow{A_iE_i}$ can be expressed in the local coordinate system $\{A_i\text{-}X_iY_iZ_i\}$ as

$$ {}^{i}\overrightarrow{A_iE_i} = {}^{i}e_i = {}^{O}\boldsymbol{R}_i^{\mathrm{T}}\left(\boldsymbol{e}_i - \boldsymbol{a}_i\right) = \begin{bmatrix} x_i & y_i & z_i \end{bmatrix}^{\mathrm{T}}. \tag{8} $$

The vector loop equation for the ith branch in the local coordinate system $\{A_i\text{-}X_iY_iZ_i\}$ is

$$ l_1\,{}^{i}\boldsymbol{m}_i + l_2\,{}^{i}\boldsymbol{n}_i = {}^{i}\mathbf{e}_i = \begin{bmatrix} x_i & y_i & z_i \end{bmatrix}^{\mathrm{T}} \tag{9} $$

where

$$ {}^{i}\boldsymbol{m}_i = \begin{bmatrix} -\cos\alpha_i & 0 & \sin\alpha_i \end{bmatrix}^{\mathrm{T}},\ {}^{i}\boldsymbol{n}_i = \left({}^{i}\mathbf{e}_i - l_1\,{}^{i}\boldsymbol{m}_i\right)/l_2. \tag{10} $$

Then

$$ l_2\,{}^{i}\boldsymbol{n}_i = {}^{i}\mathbf{e}_i - l_1\,{}^{i}\boldsymbol{m}_i. \tag{11} $$

Taking the square on both sides of Eq. (11) results in

$$ l_2^{\,2} = \left(x_i + l_1\cos\alpha_i\right)^2 + \left(z_i - l_1\sin\alpha_i\right)^2 \tag{12} $$

and Eq. (12) can be converted into

$$ \left(G_i - F_i\right)\tan^2\frac{\alpha_i}{2} + 2E_i\tan\frac{\alpha_i}{2} + \left(G_i + F_i\right) = 0 \tag{13} $$

where $E_i = -2l_1z_i$, $F_i = 2l_1x_i$ and $G_i = x_i^2 + z_i^2 + l_1^2 - l_2^2$. The solution of Eq. (13) is

$$ \alpha_i = 2\arctan\frac{-E_i \pm \sqrt{E_i^2 - G_i^2 + F_i^2}}{G_i - F_i}. \tag{14} $$

Based on Eq. (14), two solutions are available for each branch. Therefore, there are eight groups of inverse solutions for the 3-RPaS manipulator. For the configuration shown in Fig. 1, the positive sign is adopted in Eq. (14). The inverse kinematics of 3-RPaS VAPM is invariable regardless of actuation modes.

4. Performance indices for force transmissibility

The transmission performance of a PM is related to each branch chain as well as the arrangement and interaction of the branch chains on the end effector. Performance indices are defined based on the matrix orthogonal degree considering these two aspects. Assuming $\boldsymbol{X}_{m\times n} = \begin{bmatrix} \boldsymbol{x}_1 & \boldsymbol{x}_2 & \cdots & \boldsymbol{x}_n \end{bmatrix}$ is a real matrix that is composed of n real column vectors $\boldsymbol{x}_i$, the matrix orthogonal degree of $\boldsymbol{X}_{m\times n}$ is defined as follows: If $\min(\|\boldsymbol{x}_i\|) = 0\ (i = 1,2,\cdots,n)$, then the matrix orthogonal degree $ort(\boldsymbol{X})$ is zero. Otherwise,

$$ ort(\boldsymbol{X}) = \frac{vol_n(\boldsymbol{X})}{\prod_{i=1}^{n}\|\boldsymbol{x}_i\|} = \frac{\sqrt{\det(\boldsymbol{X}^{\mathrm{T}}\boldsymbol{X})}}{\prod_{i=1}^{n}\|\boldsymbol{x}_i\|} \tag{15} $$

where $vol_n(\boldsymbol{X}) = \sqrt{\det(\boldsymbol{X}^{\mathrm{T}}\boldsymbol{X})}$ is the volume of matrix $\boldsymbol{X}_{m\times n}$ in Euclidean space. When all column vectors in the matrix are unit vectors, the matrix orthogonal degree represents the volume of the n-dimensional parallel polyhedron with column vectors as its edges. The range of the matrix orthogonal degree is zero to one. The value of $ort(\boldsymbol{X})$ indicates two important geometric properties, namely, multicollinearity and orthogonality of the vectors. The maximum value of one is obtained when column vectors are orthogonal to each other. By contrast, the minimum value of zero is achieved when multicollinearity of the vectors appears.

4.1 Definition of branch transmission index

The transmission performance within a branch is described by the branch transmission index (BTI), which represents the capability of a branch to transmit driving force toward the end effector. The BTI of each branch chain depends on the transmission performance of the mounted joints. The transmission performance of a joint can be determined using the relationship between the input force applied to the joint by the former component and the output force applied to the latter component. The joint transmission index (JTI) is defined as

$$ JTI = \sqrt{1 - ort^2\left(\begin{bmatrix} \boldsymbol{f}_{\mathrm{I}} & \boldsymbol{f}_{\mathrm{O}} \end{bmatrix}\right)} \tag{16} $$

where $\boldsymbol{f}_{\mathrm{I}}$ is the input force vector and $\boldsymbol{f}_{\mathrm{O}}$ is the output force vector of the joint. When the input and output forces are collinear, the JTI value equals one. In contrast, when the input and output forces are perpendicular, the JTI value is zero. Numerically, the JTI value is equal to the cosine value of the joint pressure angle. Each branch chain generally consists of joints in series. The BTI of each branch is defined as the product of the JTIs of all the serial joints within the branch, that is,

$$ BTI = JTI_1 \times JTI_2 \times \cdots \times JTI_n \tag{17} $$

Forces of joints and components in each branch should be

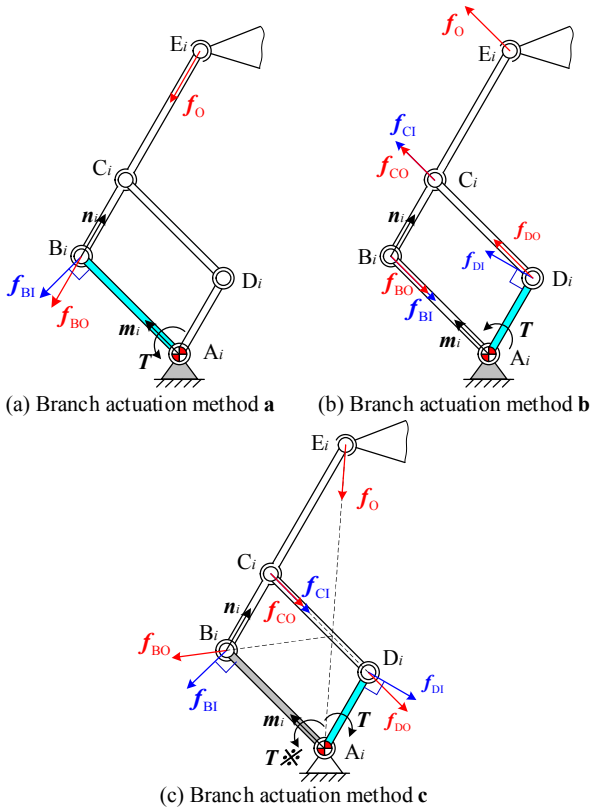

Fig. 6. Force analysis of the RPaS branch under different actuation methods.

analyzed to determine the JTI and BTI values. Force analysis of the RPaS branch under different actuation methods is shown in Fig. 6. Frictions are neglected. The calculations of BTI under different situations are analyzed as follows.

Branch actuation method **a**: As shown in Fig. 6(a), when a branch is actuated by method **a**, the driving torque is exerted on link A_iB_i, and link B_iE_i is a two-force bar. The BTI value equals the product of the JTI values of joints A_i and B_i because there is no force on joints C_i and D_i. Since the driving torque acts on link A_iB_i to drive its rotation about joint A_i, $JTI_{Ai}=1$. The input force of the joint B_i is $\boldsymbol{f}_{\mathrm{BI}}$, which is vertical to $\boldsymbol{m}_i$, and the output force $\boldsymbol{f}_{\mathrm{BO}}$ is collinear with $\boldsymbol{n}_i$, so that

$$JTI_{Bi}=\sqrt{1-ort^2\left(\left[\boldsymbol{f}_{\mathrm{BI}}\quad \boldsymbol{f}_{\mathrm{BO}}\right]\right)}=ort\left(\left[\boldsymbol{m}_i\quad \boldsymbol{n}_i\right]\right) \tag{18}$$

$$BTI_a=JTI_{Ai}\times JTI_{Bi}=ort\left(\left[\boldsymbol{m}_i\quad \boldsymbol{n}_i\right]\right). \tag{19}$$

Branch actuation method **b**: As shown in Fig. 6(b), when the branch is actuated by method **b**, the driving torque is exerted on link A_iD_i while links A_iB_i and C_iD_i are two-force bars. Since the input and output forces of joints B_i and C_i are collinear, $JTI_{Bi}=JTI_{Ci}=1$. Since the driving torque acts on link A_iD_i to drive its rotation around the joint A_i without energy loss, $JTI_{Ai}=1$. The input force of joint D_i is $\boldsymbol{f}_{\mathrm{DI}}$, which is vertical to $\boldsymbol{n}_i$, and the output force $\boldsymbol{f}_{\mathrm{DO}}$ is parallel to $\boldsymbol{m}_i$, so that

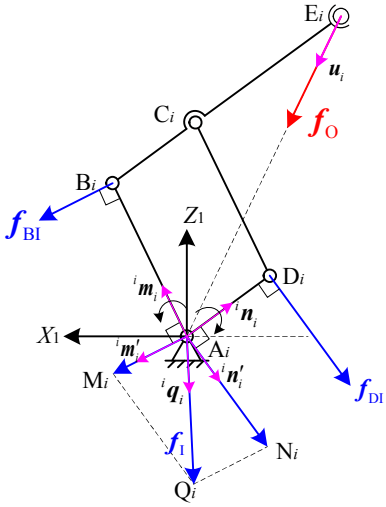

Fig. 7. Force analysis of the branch chain under actuation method **c**.

$$JTI_{Di}=\sqrt{1-ort^2\left(\left[\boldsymbol{f}_{\mathrm{DI}}\quad \boldsymbol{f}_{\mathrm{DO}}\right]\right)}=ort\left(\left[\boldsymbol{m}_i\quad \boldsymbol{n}_i\right]\right) \tag{20}$$

$$BTI_b=JTI_{Di}=ort\left(\left[\boldsymbol{m}_i\quad \boldsymbol{n}_i\right]\right). \tag{21}$$

Branch actuation method **c**: As shown in Fig. 6(c), the driving torque is applied on links A_iB_i and A_iD_i with equal value and opposite direction under actuation method **c**, generating input forces $\boldsymbol{f}_{\mathrm{BI}}$ and $\boldsymbol{f}_{\mathrm{DI}}$ at joints B_i and D_i. The equation $l_1\boldsymbol{f}_{\mathrm{BI}}=l_3\boldsymbol{f}_{\mathrm{DI}}$ always holds. The BTI of the branch is equal to the linear superposition of JTI_{Bi} and JTI_{Di}, that is,

$$BTI_c=\frac{l_3}{l_1+l_3}JTI_{Bi}+\frac{l_1}{l_1+l_3}JTI_{Di}. \tag{22}$$

The unit direction vector of E_iA_i is noted $\boldsymbol{u}_i$, and the branch force $\boldsymbol{f}_{\mathrm{O}}$ is parallel to $\boldsymbol{u}_i$. The output force $\boldsymbol{f}_{\mathrm{DO}}$ of joint D_i is parallel to $\boldsymbol{m}_i$. The output force $\boldsymbol{f}_{\mathrm{BO}}$ of joint B_i coincides with the line points from B_i to the intersection point of the lines of E_iA_i and C_iD_i. Since the computation of JTI_{Bi} is complex, we consider the branch as a whole and calculate the BTI value based on the branch input and output forces. As shown in Fig. 7, the input forces $\boldsymbol{f}_{\mathrm{BI}}$ and $\boldsymbol{f}_{\mathrm{DI}}$ are translated to A_i and synthesized to the total input force $\boldsymbol{f}_{\mathrm{I}}$ of the branch. The input force constitutes the force parallelogram $A_iM_iQ_iN_i$ that is similar to the parallelogram $A_iB_iC_iD_i$. In the local coordinate system $\{A_i\text{-}X_iY_iZ_i\}$, the direction vector of A_iM_i is ${}^i\boldsymbol{m}_i'$, and the direction vector of A_iN_i is ${}^i\boldsymbol{n}_i'$; then,

$${}^i\boldsymbol{q}_i=\frac{\overrightarrow{A_iQ_i}}{\left\|\overrightarrow{A_iQ_i}\right\|}=\frac{\boldsymbol{f}_{\mathrm{BI}}{}^i\boldsymbol{m}_i'+\boldsymbol{f}_{\mathrm{DI}}{}^i\boldsymbol{n}_i'}{\left\|\boldsymbol{f}_{\mathrm{BI}}{}^i\boldsymbol{m}_i'+\boldsymbol{f}_{\mathrm{DI}}{}^i\boldsymbol{n}_i'\right\|}=\frac{l_3{}^i\boldsymbol{m}_i'+l_1{}^i\boldsymbol{n}_i'}{\left\|l_3{}^i\boldsymbol{m}_i'+l_1{}^i\boldsymbol{n}_i'\right\|} \tag{23}$$

where ${}^i\boldsymbol{m}_i'$ can be obtained by rotating ${}^i\boldsymbol{m}_i$ around the Y_i-axis for $\pi/2$, and ${}^i\boldsymbol{n}_i'$ can be obtained by rotating ${}^i\boldsymbol{n}_i$

around the Y_i-axis for $-\pi/2$. Thus, the direction vector of the total input force $\boldsymbol{f}_1$ of the branch is collinear with $\boldsymbol{q}_i$ and

$$\boldsymbol{q}_i = {}^{O}\boldsymbol{R}_i\,{}^{i}\boldsymbol{q}_i = {}^{O}\boldsymbol{R}_i \frac{l_3\boldsymbol{R}(Y,\pi/2)^{i}\boldsymbol{m}_i + l_1\boldsymbol{R}(Y,-\pi/2)^{i}\boldsymbol{n}_i}{\left\| l_3\boldsymbol{R}(Y,\pi/2)^{i}\boldsymbol{m}_i + l_1\boldsymbol{R}(Y,-\pi/2)^{i}\boldsymbol{n}_i \right\|}. \quad (24)$$

The BTI value of the branch is

$$BTI_c = \sqrt{1-ort^2\left(\begin{bmatrix}\boldsymbol{f}_1 & \boldsymbol{f}_O\end{bmatrix}\right)} = \sqrt{1-ort^2\left(\begin{bmatrix}\boldsymbol{q}_i & \boldsymbol{u}_i\end{bmatrix}\right)}. \quad (25)$$

When BTI equals zero, the driving force of the branch cannot be transmitted to the end effector, and the end effector cannot respond to the actuation. Therefore, the manipulator loses the DOF in a certain direction and generates inverse singularity. From above analysis, it can be seen that when the parallelogram stretches into a straight line, the BTI value will be zero regardless of the branch actuation methods.

4.2 Definition of end-effector transmission index

Another aspect of the transmission performance is the combined effect of all the forces exerted on the end effector by the branches. The corresponding index is defined as the end-effector transmission index (ETI). The ETI value equals the orthogonal degree of the generalized branch force vectors that apply on the end effector, that is,

$$ETI = ort(\boldsymbol{EF}) \quad (26)$$

where $\boldsymbol{E}$ is the DOF matrix of the manipulator, and $\boldsymbol{F}$ is the matrix composed of the generalized branch force vectors. $\boldsymbol{F}$ is calculated as:

$$\boldsymbol{F} = \begin{bmatrix} \boldsymbol{f}_1 & \boldsymbol{f}_2 & \cdots & \boldsymbol{f}_n \\ \boldsymbol{r}_1 \times \boldsymbol{f}_1 & \boldsymbol{r}_2 \times \boldsymbol{f}_2 & \cdots & \boldsymbol{r}_n \times \boldsymbol{f}_n \end{bmatrix} \quad (27)$$

where $\boldsymbol{f}_i$ is the unit force vector and $\boldsymbol{r}_i \times \boldsymbol{f}_i$ is the torque vector. $\boldsymbol{r}_i$ is the unit radial vector that points from the geometric center of the end effector to the acting point of the branch force, as shown in Fig. 8. Each column vector in $\boldsymbol{F}$ describes the direction of the forces and torques generated by the unit branch forces acting on the end effector and the proportion of forces in each direction. The diagonal matrix $\boldsymbol{E} = diag\begin{pmatrix} e_1 & e_2 & e_3 & e_4 & e_5 & e_6 \end{pmatrix}$ is used for the characterization of available DOFs of the PM. e_1, e_2 and e_3 represent the translations in the X-, Y- and Z-directions, respectively, whereas e_4, e_5 and e_6 correspond to rotations around the X-, Y- and Z-axes. The corresponding element is one when the DOF is available. In contrast, if a DOF of the end effector is constrained, the corresponding element is zero. The rank of rows for matrix ($\boldsymbol{EF}$) always equals to the number of DOFs of the manipulator. It should be noted that we only study the active forces which can be generated by the actuators. The forces in the constraint space are not considered in the output transmission performance, since they are balanced by the constraint wrenches generated by mechanical constraints.

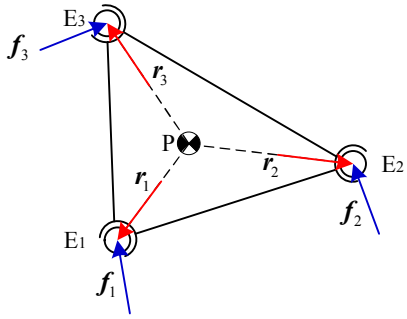

Fig. 8. Force analysis of the end effector.

ETI reflects the capability of branch force vectors to create the required output force space. In other words, ETI indicates the ability to drive the end effector's motion in the DOF space by branch output forces, or the load capability in the DOF space. When ETI equals one, the branch forces are perpendicular to each other in the DOF space, and the end effector has improved and isotropic transmission performance in all directions of motion. Two or more branch forces on the end effector are collinear if ETI equals zero, thereby leading to repeated constraints and uncontrolled DOFs. In such a case, forward singularities occur. ETI can be used for performance evaluation of all non-redundant PMs.

The spatial 3-RPaS manipulator studied in this paper has a translation along the Z-axis and two rotational DOFs around X- and Y-axes. Therefore, $\boldsymbol{E} = diag\begin{pmatrix} 0 & 0 & 1 & 1 & 1 & 0 \end{pmatrix}$. The direction of the branch force is determined by its actuation method. As shown in Fig. 6, the directions of branch forces $\boldsymbol{f}_i$ corresponding to the branch actuation methods **a**, **b** and **c** are $\boldsymbol{n}_i$, $\boldsymbol{m}_i$ and $\boldsymbol{u}_i$, respectively.

4.3 Definition of orthogonal-degree-based local transmission index

The manipulator's performance is a comprehensive effect of the interaction between branches. Therefore, the orthogonal-degree-based local transmission index (OLTI) is defined for the evaluation of the local kinematic performance of manipulators. OLTI is calculated by the product of BTI and ETI. The branch with the worst transmission performance limits the transmission performance from the actuation to the end effector. Therefore, the minimal BTI value is adopted to calculate the OLTI. Therefore,

$$OLTI = BTI_{\min} \times ETI. \quad (28)$$

If any of the BTIs or ETI is zero, the OLTI equals zero, which indicates that the manipulator is singular. By contrast, the force transmissibility of the manipulator is optimal and isotropic when OLTI equals one. It should be noted that in the

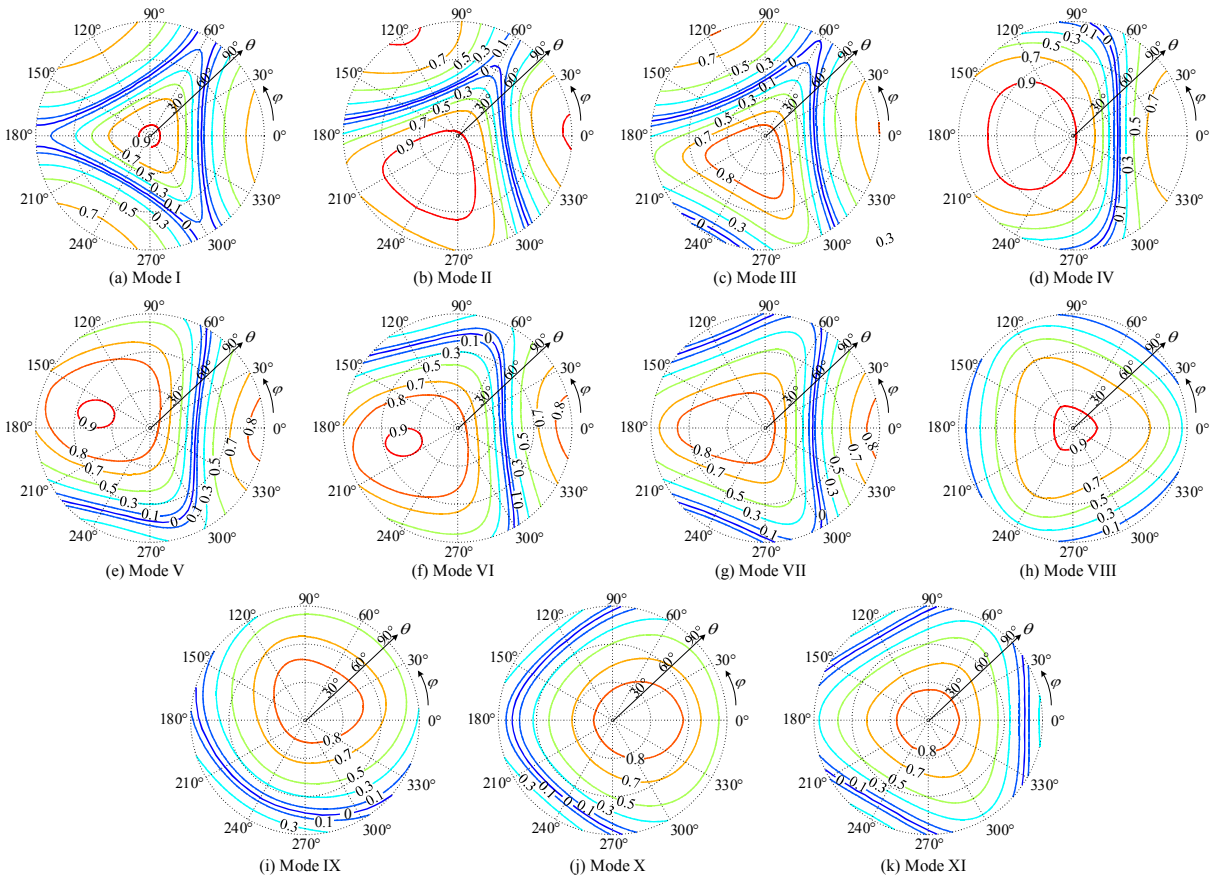

Fig. 9. OLTI atlases under different actuation modes with $Z = 700$ mm.

definitions of BTI and ETI, all parameters are dimensionless. Therefore, the orthogonality and the cross-product relationship of vectors are independent of coordinate systems. Thus, the defined performance indices possess high consistency and applicability.

5. Kinematic performance comparison under different actuation modes

Without loss of generality, the dimension parameters of the manipulator are set as $R = 250$ mm, $r = 100$ mm, $l_1 = l_2 = 500$ mm and $l_3 = 200$ mm. Fig. 9 shows the OLTI atlases of the manipulator under different actuation modes with $Z = 700$ mm.

The OLTI atlases of actuation modes I, VIII and XI exhibit 120° circumferential symmetry, and the OLTI atlases of actuation modes II, III, IV, VII, IX and X are axial symmetrical. As shown in Fig. 9, there are significant performance differences in the orientation workspace when the manipulator works under different actuation modes. The optimal regions of transmission performance under actuation modes I, VIII and XI appear in the center of the orientation workspace, while those of the other actuation modes appear off the center, and the position changes with the actuation modes.

OLTI possesses clear physical meanings and can be used to analyze the singularity. Curves of OLTI equals zero in Fig. 9 indicate the singular loci of the manipulator when $Z = 700$ mm. The singular loci of the manipulator limit the orientation capability. Fig. 10 shows the singular loci of the manipulator with the elevation of $Z = 300$ mm, 400 mm, 500 mm, 600 mm, 700 mm, 800 mm and 900 mm under different actuation modes. To fully displaying all the singular loci, θ varies from zero to π. Differences on the singularities of the 3-RPaS manipulator under different actuation modes can be further understood by analyzing and comparing the singular curves.

As shown in Fig. 10, when the 3-RPaS manipulator works under the actuation modes I to VII, the singular loci are very complicated when $Z < 500$ mm. The common feature of the seven actuation modes is that at least one branch is actuated by method **a**. Obviously, the manipulator should work in the space where $Z > 500$ mm when adopting these actuation modes. When the 3-RPaS manipulator works under actuation modes VIII, IX, X and XI, the singular loci of the manipulator are almost the same with little changes in different elevations, which indicates that the performance of the manipulator has good consistency in different elevations. When $Z = 900$ mm, the singular loci under different actuation modes are similar and complex, since the manipulator is close to the boundary of the reachable workspace and the parallelograms are nearly fully stretched.

The singular loci divide the workspace into several nonsin-

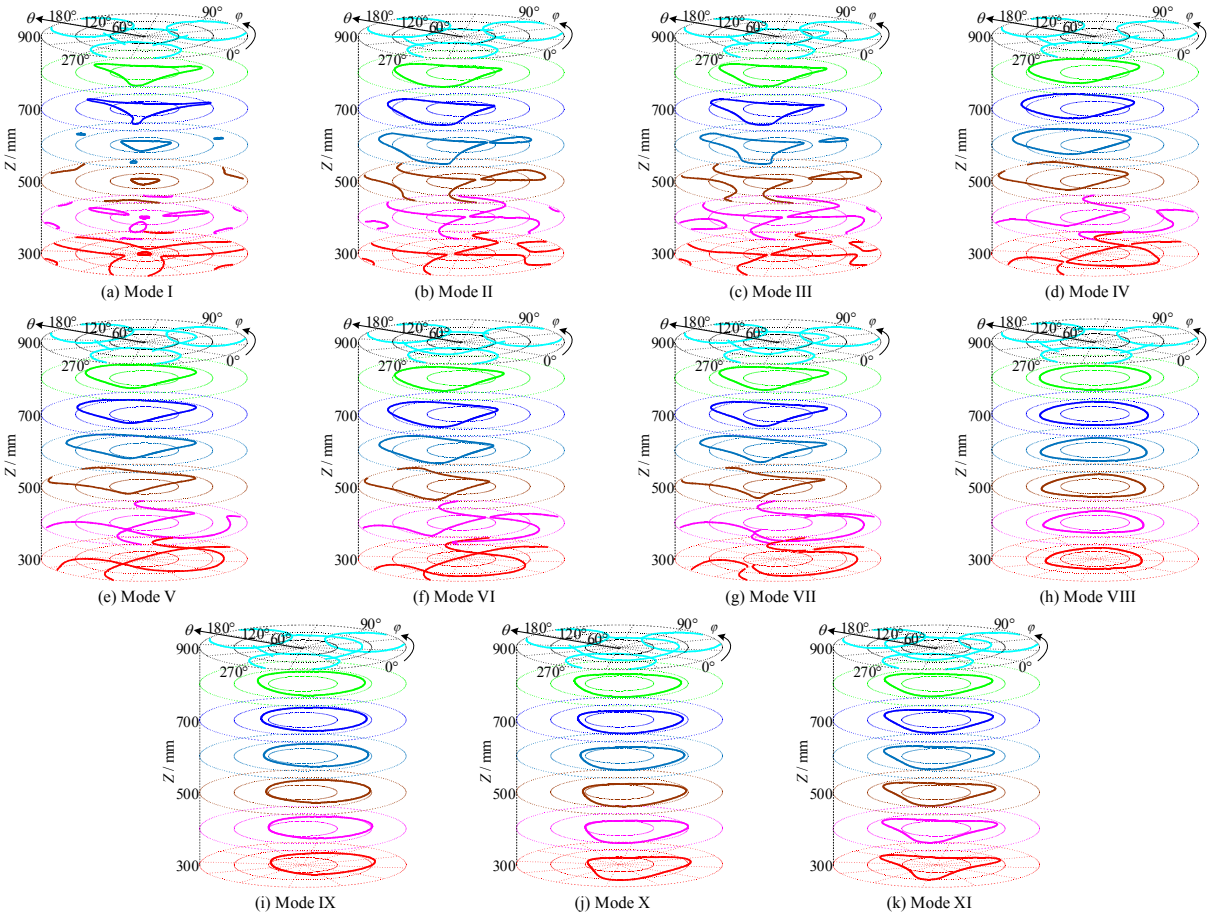

Fig. 10. Singular loci under different actuation modes when Z varies from 300 mm to 900 mm.

gular continuous areas. Normally, the manipulator cannot cross the singular loci to work in another nonsingular area. Therefore, the workspace where the manipulator can work continuously under a single actuation mode is severely limited. Fig. 11 shows the boundary shape and the variations of the nonsingular continuous workspace containing the center point between the height of Z = 500 mm and Z = 900 mm. It illustrates that the actuation mode has significant impacts on the manipulator's workspace too. In actuation mode I, the workspace of the manipulator is small, and its shape varies greatly with an increase in height. In actuation modes II to VII, the workspace of the manipulator is off the center. In actuation modes VIII to XI, the workspace is more evenly distributed around the center.

For the 2R1T PMs, the orientation capability is also important. On the orientation workspace with different Z coordinate values, there is a maximum inscribed circle centered on (0, 0) and tangent to the singular locus, as shown in Fig. 12. The radius value of the circle is defined as the isotropic orientation capability (IOC) of the manipulator. The IOC reflects the maximum tilt angle that the manipulator can achieve in all azimuths. Moreover, the maximum nonsingular tilt angle that the manipulator can achieve is defined as the maximum orientation capability (MOC). MOC represents the maximum feasible orientation capability and may only exist in one direction. The maximum values of IOC and MOC are π.

The curves of IOC with the variation of Z under different actuation modes are shown in Fig. 13. The IOC-Z curves of actuation modes I to VII are similar. The IOC value is small when Z < 400 mm, and it increases gradually with the Z coordinate value when Z > 400 mm. The IOC curves of actuation modes IX, X and XI are similar. The IOC value slowly increases with Z when Z < 860 mm and decreases rapidly when Z > 860 mm. The common feature of these three actuation modes is that at least one branch is actuated by method **c**. The IOC value of actuation mode VIII is the largest. It increases slowly with Z when Z < 850 mm, and then decreases sharply when Z > 850 mm.

The curves of MOC with the variation of Z under different actuation modes are shown in Fig. 14. The MOC curves of actuation modes II to VII are similar. In the range of Z = 320 mm to 510 mm, the MOC values reach the maximum value π. When Z > 510 mm, the MOC values decrease as Z increases. The MOC curves of actuation modes IX, X and XI are similar in the trends, which slowly decrease as Z increases. The MOC value of actuation mode VIII is the minimum, and so is the value variation. The MOC curve of actuation mode I is special. When the Z is small, the MOC value is very small. Then, it

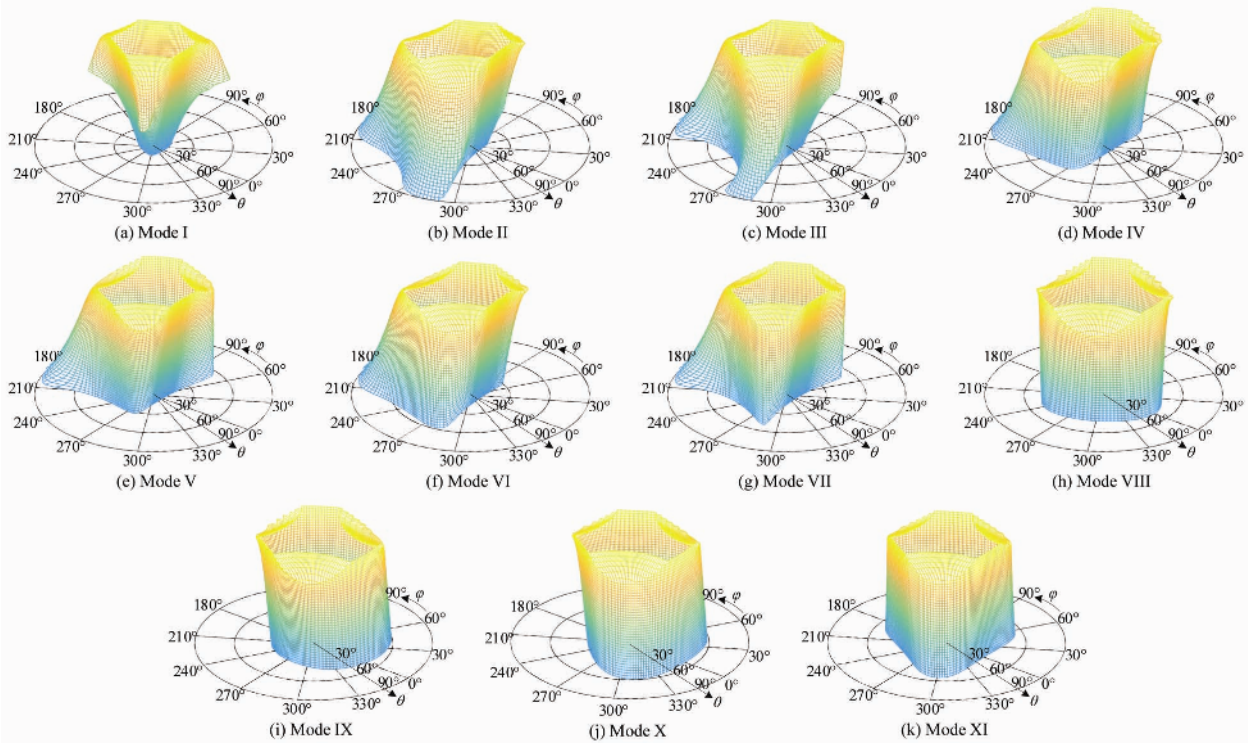

Fig. 11. The boundaries and the variations of the nonsingular continuous workspace.

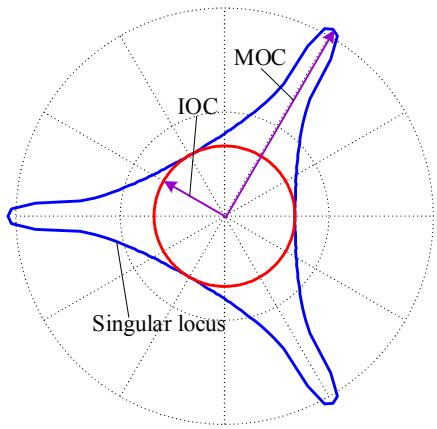

Fig. 12. Definition of IOC and MOC.

rises rapidly with the increase in Z, reaches the peak at Z = 700 mm, and then drops.

The IOC value is small and the MOC value is large if there is one or more branch actuated by method **a**. In contrast, the IOC value is the largest and the MOC value is the smallest if all the three branches are actuated by method **b**. The greater the difference between MOC and IOC, the more obvious the directionality of the orientation capability is. Better performance of the 3-RPaS manipulator can be obtained through reasonable selection of the actuation mode according to the requirements of specific tasks. If the tasks performed by the manipulator have obvious directionality or asymmetry, such as the solar tracker, the actuation modes I to VII can be used correspondingly. When all the branches are actuated by method **b** or **c**, the orientation capabilities of the manipulator are relatively uniform in different azimuths, and the performance of the manipulator is more isotropic. The corresponding actuation modes VIII to XI can be used in the application of tool heads, motion simulators, and measuring machines.

The traditional 3-RRS spatial PM is equivalent to the 3-RPaS PM that works under actuation mode I. According to the above analysis, the transmission performance of 3-RRS PM is poor, and the workspace is small, which limits its application. Compared with the 3-RRS manipulator, the proposed 3-RPaS manipulator has a variety of actuation modes to choose. By changing the actuation modes, the kinematic performance can be greatly adjusted and improved.

6. Improve the kinematic performance via actuation mode conversion

It can be seen from Figs. 9-11 that there are significant differences in performance when the 3-RPaS manipulator works under different actuation modes at a given position. To obtain the best kinematic performance, the 3-RPaS manipulator shall optimize the actuation mode. In other words, the 3-RPaS manipulator should convert its actuation modes in real-time according to the position and orientation of the end effector, and the manipulator always behaves with the optimal performance. The actuation mode that maximizes the OLTI value at a given position is referred to the optimal actuation mode for that position. Fig. 15(a) shows the distribution and conversion map of the optimal actuation modes when Z = 700 mm. The OLTI

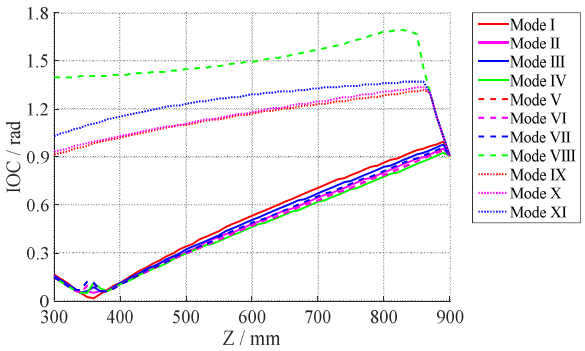

Fig. 13. Relation of IOC value and Z coordinate value.

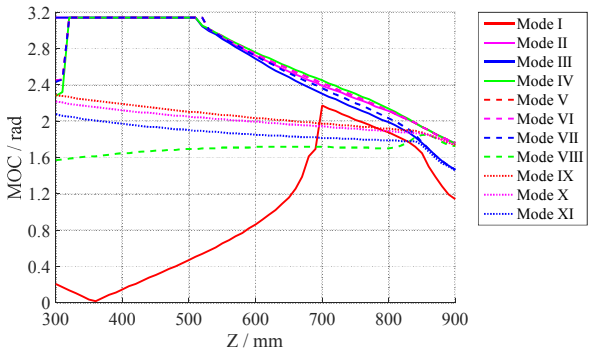

Fig. 14. Relation of MOC and Z under different actuation modes.

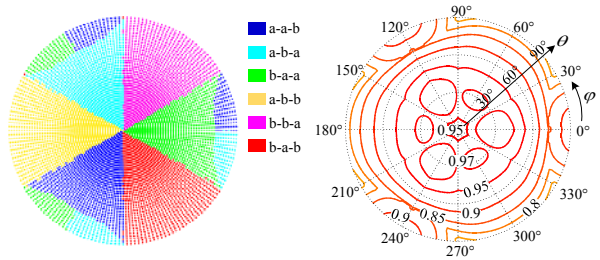

(a) Conversion map of optimal modes (b) OLTI atlas under optimal modes

Fig. 15. Conversion map of optimal modes and OLTI atlas under optimal modes.

atlas when the manipulator works under optimal actuation modes via actuation mode conversion is shown in Fig. 15(b). By comparing Fig. 15(b) and Fig. 9, we can conclude that the transmission performance of the 3-RPaS manipulator is significantly improved with optimal actuation modes. Moreover, the workspace is greatly increased, and singularities no longer appear inside the workspace. Actuation mode conversion is a potential way to improve the kinematic performance of parallel manipulators without changing the topology and parameters.

To obtain the conversion of actuation modes in practical applications, a conversion module is designed to switch the applied position of driving and reaction torques in real-time. The purpose is achieved by switching the connection relationship of the motor and links in real-time. Electromagnetic clutches and brakes can control the connection and separation

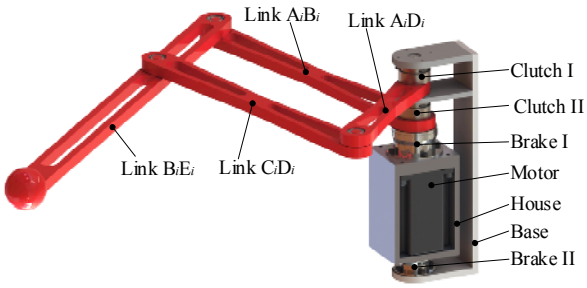

Fig. 16. The variable actuated RPaS branch chain.

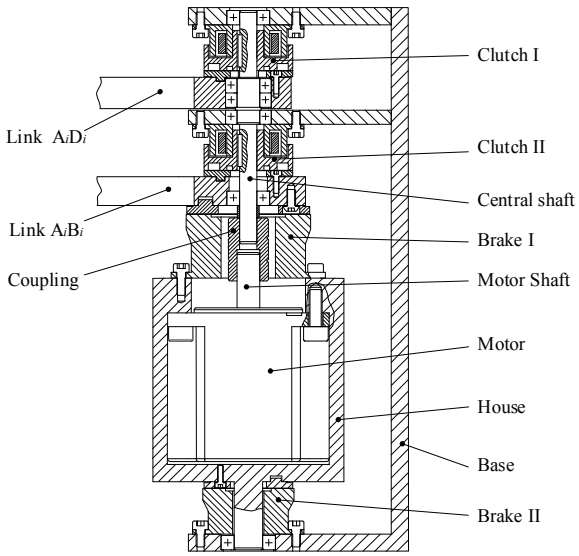

Fig. 17. The detailed design of the actuation mode conversion module.

of yokes and armatures in real time through electrical signals, which can be utilized in the real-time transformation of the connection of the motor shell and the output shaft with different components. In this study, two electromagnetic clutches and two electromagnetic brakes are used, and a design scheme of the mode conversion module is demonstrated. Fig. 16 shows the appearance of a variable actuated RPaS branch chain. Fig. 17 shows the design and assembly drawing in details. Two electromagnetic brakes are installed on both sides of the motor and used to switch the connection of the motor shell. Two electromagnetic clutches are coaxially mounted on the central shaft and used to switch the applied position of the driving force. By controlling electromagnetic clutches and brakes, the transmission path of driving and reaction torques can be changed. The conversion principle of the module is detailed below.

(1) When brake I and clutch I are disengaged while brake II and clutch II are engaged, the motor shell is connected to the base and the output shaft is connected with link A_iB_i. The driving torque acts on link A_iB_i, and the reaction torque acts on the base. Branch actuation method **a** is implemented.

(2) When brake I and clutch II are disengaged while brake II and clutch I are engaged, the motor shell is connected to the base and the output shaft is connected with link A_iD_i. The

driving torque acts on link A_iD_i, and the reaction torque acts on the base. Branch actuation mode **b** is implemented.

(3) When brake I and clutch I are engaged while the brake II and clutch II are disengaged, the motor shell is connected with link A_iB_i and the output shaft is connected with link A_iD_i. The driving torque acts on link A_iD_i while the reaction torque acts on link A_iB_i. Branch actuation mode **c** is implemented.

When all the brakes and clutches are engaged, the RPaS branch chain is locked and cannot rotate anymore. In addition to the above four combinations, the other combinations are in an abnormal working status and should be avoided in practical applications.

Depending on the parameters and workspace of the manipulator, it may not necessary to use all three of the actuation methods for an RPaS branch. As the example shows in Fig. 15(a), branch actuation method **c** is not used in the optimal actuation modes. In this case, the mode conversion module can be simplified. Two electromagnetic brakes can be removed, and the motor shell can be fixed to the base. The function of actuation mode conversion can be realized with two clutches to switch the applied position of driving torque to link A_iB_i or A_iD_i.

7. Conclusions

This paper proposed a 3-RPaS spatial PM with parallelograms, which can realize the 2R1T motion. By changing the connection between the motor and the different links of the parallelogram, the 3-RPaS manipulator can implement 27 actuation modes. The inverse kinematics of the 3-RPaS manipulator were established. The T&T angle was used to describe the orientation of the end effector. To explore the differences and characteristics of the transmission performance of 3-RPaS manipulator under different actuation modes, the transmission indices BTI, ETI and OLTI were defined based on the concept of matrix orthogonal degree. Based on the OLTI index, the kinematic performance, including the singularity and orientation capability, of the 3-RPaS manipulator under different actuation modes was analyzed and compared. The results show that when branch actuation method **a** was used, the performance of the manipulator appears to have obvious directionality. When the branches of the manipulator are actuated by method **b** or **c**, the transmission performance tends to be more isotropic. The differences and complementarity in transmission performance under different actuation modes provide a new way to improve the performance. The concept of optimal actuation modes and the approach of actuation mode conversion were proposed. An implementation scheme of the actuation mode conversion module was designed for the 3-RPaS manipulator. By converting the corresponding optimal actuation mode according to the position and orientation of the end effector in real-time, the transmission performance of the 3-RPaS manipulator can be significantly promoted, and forward singularity can be eliminated. Actuation mode conversion is an efficient way to improve the kinematic performance of parallel manipulators.

Acknowledgments

This work was supported by the National Natural Science Foundation of China (grant number 51575292) and National Science and Technology Major Project of the Ministry of Science and Technology of China (grant number 2016ZX04004004, 2018ZX04020001). The authors would like to thank the editor and reviewers for their pertinent comments and suggestions.

References

[1] J. Mo, Z. F. Shao, L. Guan, F. Xie and X. Tang, Dynamic performance analysis of the X4 high-speed pick-and-place parallel robot, *Robotics and Computer-Integrated Manufacturing*, 46 (2017) 48-57.

[2] X. Duan, Y. Yang and B. Cheng, Modeling and analysis of a 2-DOF spherical parallel manipulator, *Sensors*, 16 (9) (2016) 1485.

[3] F. Pierrot, C. Reynaud and A. Fournier, DELTA: A simple and efficient parallel robot, *Robotica*, 8 (2) (1990) 105-109.

[4] J. Wahl, Articulated tool head, *US Patent*, 6431802B1 (2002).

[5] X. Chen, X. J. Liu, F. Xie and T. Sun, A comparison study on motion/force transmissibility of two typical 3-DOF parallel manipulators: The sprint Z3 and A3 tool heads, *International Journal of Advanced Robotic Systems*, 11 (1) (2014) 1-10.

[6] F. Xie, X. J. Liu, Z. You and J. Wang, Type synthesis of 2T1R-type parallel kinematic mechanisms and the application in manufacturing, *Robotics and Computer-Integrated Manufacturing*, 30 (1) (2014) 1-10.

[7] D. Wang, J. Wu and L. Wang, Research on the error transfer characteristics of a 3-DOF parallel tool head, *Robotics and Computer-Integrated Manufacturing*, 50 (2018) 266-275.

[8] J. Wu, X. Chen and L. Wang, Design and dynamics of a novel solar tracker with parallel mechanism, *IEEE/ASME Transactions on Mechatronics*, 21 (1) (2016) 88-97.

[9] B. Hu, L. Zhang and J. Yu, Kinematics and dynamics analysis of a novel serial-parallel dynamic simulator, *Journal of Mechanical Science & Technology*, 30 (11) (2016) 5183-5195.

[10] J. Yu, Y. Hu, S. Bi, G. Zong and W. Zhao, Kinematics feature analysis of a 3 DOF in-parallel compliant mechanism for micro manipulation, *Chinese Journal of Mechanical Engineering*, 17 (1) (2004) 127-131.

[11] D. Liu, R. Che, Z. Li and X. Luo, Research on the theory and the virtual prototype of 3-DOF parallel-link coordinating measuring machine, *IEEE Transactions on Instrumentation and Measurement*, 52 (1) (2003) 119-125.

[12] Y. Song, P. Han and P. Wang, Type synthesis of 1T2R and 2R1T parallel mechanisms employing conformal geometric algebra, *Mechanism and Machine Theory*, 121 (2018) 475-486.

[13] Y. D. Xu, D. S. Zhang, J. T. Yao and Y. S. Zhao, Type

synthesis of the 2R1T parallel mechanism with two continuous rotational axes and study on the principle of its motion decoupling, *Mechanism and Machine Theory*, 108 (2017) 27-40.

[14] L. Xu, Q. Li, J. Tong and Q. Chen, Tex3: An 2R1T parallel manipulator with minimum DOF of joints and fixed linear actuators, *International Journal of Precision Engineering and Manufacturing*, 19 (2) (2018) 227-238.

[15] B. Hu and Z. Huang, A family of 2R1T parallel manipulators with intersecting rotational axes, X. Ding et al. (Eds.), *Advances in Reconfigurable Mechanisms and Robots II*, Springer International Publishing, Switzerland (2016) 287-295.

[16] Y. Xu, S. Zhou, J. Yao and Y. Zhao, Rotational axes analysis of the 2-RPU/SPR 2R1T parallel mechanism, M. Ceccarelli and V. A. Glazunov (Eds.), *Advances on Theory and Practice of Robots and Manipulators, Mechanisms and Machine Science*, Springer International Publishing, Switzerland (2014) 113-121.

[17] D. Wang, R. Fan and W. Chen, Performance enhancement of a three-degree-of-freedom parallel tool head via actuation redundancy, *Mechanism and Machine Theory*, 71 (1) (2017) 142-162.

[18] L. Xu, Q. Li, N. Zhang and Q. Chen, Mobility, kinematic analysis, and dimensional optimization of new three-degrees-of-freedom parallel manipulator with actuation redundancy, *Journal of Mechanisms and Robotics*, 9 (2017) 041008.

[19] S. H. Cha, T. A. Lasky and S. A. Velinsky, Singularity avoidance for the 3-RRR mechanism using kinematic redundancy, *2007 IEEE International Conference on Robotics and Automation* (2007) 1195-1200.

[20] L. Wang, H. Xu and L. Guan, Optimal design of a 3-PUU parallel mechanism with 2R1T DOFs, *Mechanism and Machine Theory*, 114 (2017) 190-203.

[21] N. Rakotomanga, D. Chablat and S. Caro, Kinetostatic performance of a planar parallel mechanism with variable actuation, J. Lenarcic and P. Wenger (Eds.), *Advances in Robot Kinematics: Analysis and Design*, Springer, Dordrecht (2008) 311-320.

[22] Z. Zhang, L. Wang and Z. Shao, Improving the kinematic performance of a planar 3-RRR parallel manipulator through actuation mode conversion, *Mechanism and Machine Theory*, 130 (2018) 86-108.

[23] L. Wang, Z. Zhang, Z. Shao and X. Tang, Analysis and optimization of a novel planar 5R parallel mechanism with variable actuation modes, *Robotics and Computer-Integrated Manufacturing*, 56 (2019) 178-190.

[24] H. Qu, Y. Fang and S. Guo, A new method for isotropic analysis of limited DOF parallel manipulators with terminal constraints, *Robotica*, 29 (4) 563-569.

[25] T. Yoshikawa, Manipulability of robotic mechanisms, *International Journal of Robotics Research*, 4 (2) (1985) 3-9.

[26] C. Gosselin and J. Angeles, The optimum kinematic design of a spherical three-degree-of-freedom parallel manipulator, *Journal of Mechanical Design*, 111 (2) (1989) 202-207.

[27] C. Gosselin and J. Angeles, A global performance index for the kinematic optimization of robotic manipulators, *Journal of Mechanical Design*, 113 (3) (1991) 220-226.

[28] J. P. Merlet, Jacobian, manipulability, condition number and accuracy of parallel robots, *Journal of Mechanical Design*, 128 (1) (2005) 199-206.

[29] X. J. Liu, C. Wu and J. Wang, A new index for the performance evaluation of parallel manipulators: A study on planar parallel manipulators, *Proceedings of the 7th World Congress on Intelligent Control and Automation* (2008) 353-357.

[30] R. S. Ball, *A treatise on the Theory of Screws*, Kessinger Publishing, Montanna (2007).

[31] M. S. C. Yuan, F. Freudenstein and L. S. Woo, Kinematics analysis of spatial mechanism by means of screw coordinates, Part 2—Analysis of spatial mechanisms, *Journal of Manufacturing Science and Engineering*, 93 (1) (1971) 67-73.

[32] G. Sutherland and B. Roth, A transmission index for spatial mechanisms, *Journal of Manufacturing Science and Engineering*, 95 (2) (1973) 579-587.

[33] M. J. Tsai and H. W. Lee, The transmissivity and manipulability of spatial mechanisms, *Journal of Mechanical Design*, 116 (1) (1994) 137-143.

[34] M. J. Tsai and H. W. Lee, Generalized evaluation for the transmission performance of mechanisms, *Mechanism and Machine Theory*, 29 (4) (1994) 607-618.

[35] C. Chen and J. Angeles, Generalized transmission index and transmission quality for spatial linkages, *Mechanism and Machine Theory*, 42 (9) (2007) 1225-1237.

[36] J. Wang, C. Wu and X. J. Liu, Performance evaluation of parallel manipulators: Motion/force transmissibility and its index, *Mechanism and Machine Theory*, 45 (10) (2010) 1462-1476.

[37] Z. F. Shao, J. Mo, X. Q. Tang and L. P. Wang, Transmission index research of parallel manipulators based on matrix orthogonal degree, *Chinese Journal of Mechanical Engineering*, 30 (6) (2017) 1396-1405.

[38] J. Li, J. Wang, W. Chou and Y. Zhang, Inverse kinematics and dynamics of the 3-RRS parallel platform, *Proceedings of 2011 IEEE International Conference on Robotics and Automation*, 3 (2001) 2506-2511.

[39] X. J. Liu and I. A. Bonev, Orientation capability, error analysis, and dimensional optimization of two articulated tool heads with parallel kinematics, *Journal of Manufacturing Science & Engineering*, 130 (1) (2008) 011015.

Liping Wang received his Ph.D. degree in Mechanical Engineering from Jilin University of Technology, China, in 1997. He is currently a Professor of Tsinghua University, China. His research interests include advanced manufacturing equipment and its control, mechanism theory and control of parallel robots.

Zhaokun Zhang received his bachelor's degree in Mechanical Engineering from Huazhong University of Science and Technology, China, in 2015. He is currently a Ph.D. candidate at Tsinghua University, China. His research interests include intelligent manufacturing, parallel robots, and cable-driven parallel robots.

Zhufeng Shao received his bachelor's degree from Shandong University, China, in 2006 and Ph.D. degree in Mechanical Engineering from Tsinghua University, China, in 2011. He is currently an Associate Professor of Tsinghua University. His research interests include advanced manufacturing equipment and its control, rigid-flexible coupling system, and cable robots.